ELSEVIER

Contents lists available at ScienceDirect

Materials Chemistry and Physics

journal homepage: www.elsevier.com/locate/matchemphys





Boosting lithium polysulfide conversion via TiO₂-supported niobium catalyst for lithium sulfur battery

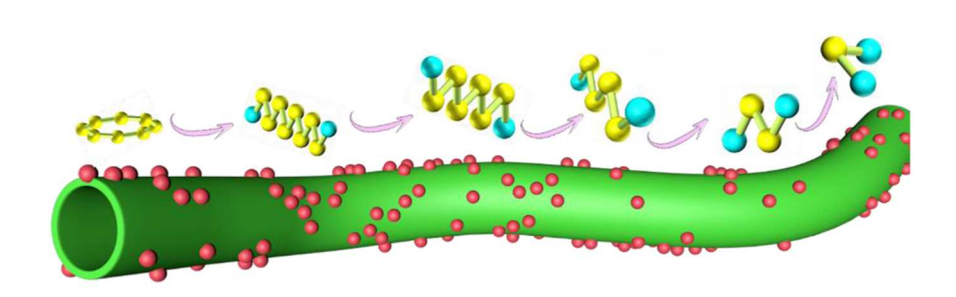
Zephyr Barlow¹, Zhen Wei¹, Ruigang Wang^{*}

Department of Metallurgical and Materials Engineering, The University of Alabama, Tuscaloosa, AL, 35487, USA

HIGHLIGHTS

- Surface and defect engineered TiO₂ supported Nb catalysts for mitigating lithium polysulfide shuttle.
- Synergistic effects of physical confinement, chemical binding adsorption, and catalysis.
- Robust 3D hierarchical structure for accelerated polysulfides conversion.

GRAPHICAL ABSTRACT



Effective trapping and rapid conversion of sulfur species via TiO₂-supported Nb catalyst

ARTICLE INFO

Keywords: Lithium sulfur battery Host materials Polysulfides conversion Catalytic effect Niobium catalyst

ABSTRACT

Lithium sulfur (Li–S) batteries demonstrate enormous promise as a high-performance high-capacity energy storage solution but are severely limited by a low cycle life which stems from rapid capacity decay due to the low conductivity of lithium polysulfides and the poor kinetics of the lithium sulfur reduction reaction, which combined lead to the loss of active cathodic material. In this work, titanium oxide (TiO₂) nanostructures are used as a host for a niobium catalyst which accelerates the conversion of polysulfides. Cells containing the TiO₂-supported niobium catalyst demonstrated a very high level of stability, with a specific capacity decay rate of 0.045 % per cycle over 350 cycles. Li–S cells using this cathode host material also demonstrated high initial specific capacities, with initial capacities as high as 961 mAh $\rm g^{-1}$ at 0.2 C and 629 mAh $\rm g^{-1}$ at 3.0 C.

^{*} Corresponding author.

E-mail address: rwang@msu.edu (R. Wang).

 $^{^{1}}$ contributed equally to this work.

1. Introduction

A shift in the current paradigm of procuring energy from fossil fuels to the use of cleaner, sustainable sources is a global solution to meeting the world's increasing energy needs while protecting the environment [1-5]. Among environmentally friendly and sustainable energy storage systems, rechargeable batteries [6-8] and supercapacitors [9-12] have been receiving increasing attention recently. With the energy density of the Li-ion battery approaching its theoretical maximum, the scientific community has recently shifted their interest to systems beyond Li-ion. Due to the abundance and low cost of elemental sulfur, the lithium-sulfur (Li-S) battery has been recognized as a promising candidate for the next generation of energy storage. Unfortunately, the poor kinetics of the lithium sulfur (Li-S) reduction reaction currently limit the practical performance of Li-S batteries, however, they can be improved through the use of Nb catalysts on cathode host materials. Various materials [13-15] (such as metal oxides and metal sulfides, etc) have been reported to be considered as catalysts for polysulfide conversion. Metal oxides have been extensively applied in rechargeable Li-S batteries owing to their impressive adsorption capability, which can immobilize polysulfides and mitigate the shuttle effect effectively. However, metal oxides demonstrate a low conductivity and a limited capability to promote the kinetics of polysulfide redox chemistry. Considering the complicated multi-step chemical reactions and sluggish redox kinetics, accelerating the chemical conversion of sulfur species is of great significance for the alleviation of sulfur losses. Electrocatalysis can serve to remedy this, as they have a significant impact on regulating the redox rate. When loaded on the TiO2-based nanotubes, Nb catalysts act as extremely polar sites, a property which gives them several capabilities. Firstly, Nb catalysts are able to further increase the conductivity of cathode host materials, improving the rate of electron transfer and the speed at which the Li-S reduction reaction can occur. In particular, catalysts promote the kinetics of the slow liquid to solid phase and solid to solid phase changes experienced during the discharge of Li-S cells [16]. Secondly, Nb catalysts are able to act as a polar host for lithium polysulfides (LiPS), reducing the severity of the polysulfide shuttling effect by limiting the mobility of liquid LiPS and preventing its diffusion to the anode. Thirdly, the bonds formed between Nb catalysts and LiPS weaken the S-S bonds of the sulfur chains, reducing the energy needed for reduction [17]. A wide variety of different catalysts have been analyzed, via both simulation and experimentation, and results indicate that d-block metals of the fourth period demonstrate the best performance as catalysts for the cathode side of Li-S batteries. Among these, niobium has been identified as especially potent. Niobium and sulfur have the following electron configurations, [Kr] 4 d⁴ 5s¹ and [Ne] 3s² 3p⁴ respectively. Theoretical analysis indicates that Nb catalysts should promote d-p hybridization, enhancing the ability of a host material to trap LiPS. The p orbital of the sulfur atoms in the LiPS chain overlaps with the d orbital of the Nb catalysts, resulting in the formation of π and σ bonding states. This results in the hybrid d-p orbital state experienced by the two atoms, which serves to improve the ability of Nb catalysts to adsorb LiPS. The reduction of the adsorbed LiPS is then spurred by the enhanced charge transfer kinetics and conductivity of the host material due to the presence of the Nb catalysts [18].

Electrochemical catalysts require a substrate and demonstrate the best performance when paired with a host material that already improves the performance of Li–S batteries. TiO₂-based nanotubes are one such material and present some unique advantages when paired with catalysts and with Nb catalysts specifically [19].

On their own, TiO_2 based cathode host materials have shown great promise. TiO_2 was identified early in the recent development of Li–S cathode host materials as an excellent candidate due to its ability to readily adsorb and trap liquid phase LiPS [20]. TiO_2 is an extremely stable material, able to demonstrate many different morphologies and withstand chemical treatments. The adsorptive capability of TiO_2 can be further enhanced through surface engineering to increase surface area

and through the introduction of oxygen deficiencies which increase the material's affinity for LiPS [21]. Increasing the surface area to volume ratio of the material increases the amount of LiPS the $\rm TiO_2$ can interact with, while the introduction of oxygen vacancies and other defects increases the strength of the interaction. These coupled factors cause high surface area oxygen deficient $\rm TiO_2$ materials to demonstrate a catalytic effect on the Li–S reduction reaction, as the increased surface contact of the adsorbed LiPS enables easier electron transfer to and from the cathodic material.

The phenomena demonstrated by the defects caused by oxygen deficiencies in TiO2 can be further enhanced through the use of Nb as a doping agent to introduce larger scale defects. Ti and Nb both share very similar atomic radii, 0.70 Å and 0.68 Å respectively, meaning that the lattice mismatch between TiO2 and Nb2O5 has little impact on the structure of the hybrid metal oxide [22]. This trend remains true for the ions of Nb and Ti found in metal oxides, with the ionic radii of Ti⁴⁺, Ti³⁺ and Nb^{5+} being 0.605 Å, 0.670 Å and 0.64 Å respectively [23,24]. The introduction of Nb catalyst into TiO2 lattices also promotes the formation of Ti³⁺ and Ti vacancies due to the differing valance of the two metals (Nb5+, Ti4+), leading to increased electrical conductivity [25]. The formation of these Ti vacancies due to the Nb doping also causes the ion diffusion channels within the structure of TiO2 to expand, further increasing the adsorptive capabilities of the host material [26]. The use of TiO2-based nanotubes as a substrate for Nb catalyst loading would bolster the catalytic and polar host properties of both materials, leading to the formation of a cathode host material with superior performance.

2. Experimental

2.1. Preparation of TiO2-based nanotubes

TiO2-based nanotube samples were prepared via a one-step hydrothermal template synthesis method [27]. The samples were prepared from rutile TiO2 (predominantly rutile titanium (IV) oxide, 99.999 %, Acros Organics). The initial particle size of TiO2 material has a significant impact on the final morphology of the nanotube structure, with larger initial particle sizes leading to longer and more ordered nanotubes. 2 g of the rutile TiO_2 powder was added to 80 mL of 10 M NaOH solution. The mixture was vigorously magnetically stirred for 24 h at ambient temperature to ensure the TiO₂ powder was totally dissolved. The solution was then placed in a 200 mL Teflon lined autoclave and sealed. Nanotube formation was performed using a programable box furnace, which heated the sample and held it at 150 °C for 72 h. The sample was allowed to air cool to ambient temperature in the box furnace. The TiO2-based nanotube slurry was poured into a vacuum filtration center, and any solids were scraped out of the autoclave into the vacuum filter as well. The solids were first washed with a 40 mL 0.1 M HCl solution, and then with 500 mL DI water. The HCl solution is meant to remove sodium ions left on the nanostructure from the NaOH solution by causing them to interact with Cl ions in solution rather than the TiO₂ crystal, and the DI water wash is meant to dissolve and remove the resulting ions from the surface of the nanostructure [28]. The solids were then removed from the filter and placed in a vacuum furnace set at 80 °C to dry overnight.

2.2. Preparation of Nb catalyst loading on TiO2-based nanotube

Nb catalysts were loaded onto TiO_2 -based nanotubes via a modified two-step chemical/thermal method [18]. Nb precursor was first loaded onto the TiO_2 -based nanotubes via the mixing in absolute ethanol in an argon-filled glove box. 0.15 g TiO_2 -based nanotube powder was added to 50 mL absolute ethanol and agitated via magnetic stirring in an Erlenmeyer flask until fully dispersed. Once dispersed, $10.5~\mu L$ of niobium ethoxide (99.9 %, Strem Chemicals INC) was added slowly under continued agitation. Once the niobium ethoxide had been fully dispersed, the flasks were sealed shut via rubber stoppers and parafilm,

then removed from the glove box and stirred overnight. The resulting suspension of niobium ethoxide loaded TiO_2 particles was then filtered using a vacuum filter and $0.22~\mu m$ pore size nylon membrane filters and allowed to dry in a desiccator. Once totally dry, the loaded TiO_2 -based nanotube was placed in ceramic crucibles and moved to a tube furnace. This tube furnace was heated to 960 °C for 3 h under flowing argon gas. The samples were allowed to cool to ambient temperature in an argon atmosphere. A sample without niobium catalyst loading (TiO_2 -based nanotube) was created to act as a control sample.

2.3. Preparation of electrolyte solution and Li₂S₆ catholyte solution

The electrolyte solution was prepared by combining 2 mL dioxolane (DOL) with 2 mL dimethoxyethane (DME) to create 1:1 ratio DOL:DME solution (Alfa Aesar, 99 %). 1.15 g lithium bis(trifluoromethane) sulfonimide (LiTFSI) (AdipoGen Life Sciences, 99 %) and 0.15 g lithium nitrate (Alfa Aesar, 99.999 %) were then added to the solution. The solution was stirred at ambient temperature for 24 h [29]. All mixing and stirring were performed in an argon-filled glove box due to the oxygen and moisture sensitivity of the electrolyte and its components.

 ${\rm Li}_2S_6$ was used as the active material in the catholyte solution due to the fact that it is soluble in the electrolyte and can be prepared via a facile synthesis method. Its liquid nature allows it to easily be applied to the electrode via the use of a micropipette and allows it to be quickly and deeply adsorbed by the host material due to the high kinetic mobility of liquids rather than applied as a powder to the surface of the electrode. The catholyte was prepared by adding 92 mg ${\rm Li}_2S$ (Alfa Aesar, 99.9 %) and 320 mg sublimed elemental sulfur powder (Alfa Aesar, 99.5 %) to 2 mL of the electrolyte solution to create a 1.0 ${\rm Li}_2S_6$ solution. The solution was stirred for 24 h at 60 °C to enable the formation of ${\rm Li}_2S_6$ from ${\rm Li}_2S$ and sulfur [30].

2.4. TiO2 on carbon cloth electrode preparation

Cathodes were prepared by applying TiO2-supported niobium catalyst or TiO2-based nanotube containing slurry to 15 mm carbon cloth discs (Fuel cell earth, thickness = 0.381 mm, density = 1.75 g/cm^3). The slurries were prepared by combining 50 mg of the TiO2-supported niobium catalyst or TiO2-based nanotube with 7.5 mg super P carbon black (Alfa Aesar, 99 %) and 7.5 mg polyvinylidene fluoride (PVDF). The powder mixture was then added to $600~\mu L$ N-methyl-2-pyrrolixone (NMP). In this mixture, the super P acts to boost the conductivity of the cathode host, the PVDF acts as a thermosetting binder, and the NMP acts as a solvent for the three powders. The slurry was then stirred vigorously for 24 h to ensure even dispersion of all three powders. The prepared slurry was then applied to carbon cloth discs via a micropipette, with 30 μL applied to each disc. This volume was chosen as it results in the application of between 2.0 and 3.0 mg of host material, which was found to show the best results. The cathode host loaded carbon cloth electrode discs were then dried in a vacuum furnace set at 60 °C for 24 h.

2.5. Cell assembly

Cell assembly was performed in an argon-filled glove box using the previously prepared materials, lithium metal foil discs, Celgard 2500 separators, commercially available stainless steel CR2032 size coin cell casings, spacers, and springs. Cell assembly started by placing the cathode host loaded carbon cloth electrode on the positive side cell casing and centering it. 10 μL of the catholyte, corresponding to an areal loading of 1 mg cm $^{-2}$ active sulfur on the electrode, was then applied to the center of the electrode. 30 μL of the electrolyte was then applied to the center of the electrode. A 19 mm disc of Celgard 2500 separator material was then placed to isolate the cathodic and anodic sides of the cell. Another 30 μL of electrolyte was applied to the center of the anodic side of the separator. A lithium metal anode disc was placed on top of the electrolyte at the center of the cell, followed by a spacer and a spring.

The negative case was then fitted over the lithium metal anode and spacers, and the cell was crimped closed using a die and 100 kg cm^{-2} of force applied via a manual hydraulic press.

2.6. Electrochemical testing

Electrochemical impedance spectroscopy (EIS) testing, cyclic voltammetry (CV) testing, and galvanostatic charge discharge cycling were performed on Li–S cells containing the TiO₂-supported niobium catalyst or TiO₂-based nanotube. EIS testing was conducted to assess the internal resistance of each cell, CV testing was conducted to determine the relative voltage and current peaks of charge and discharge cycles and impact of the catalytic materials, and charge discharge cycling was conducted to determine the stability of the cathode host at different current rates and over time. A Gamry Interface 1000E potentiostat/galvanostat/ZRA instrument was used to perform EIS and CV measurements. Charge discharge cycling was performed using a Neware battery testing system.

2.7. Materials characterization

XRD analysis was performed using a Philips X'Pert MRD with a Cu K α source (wavelength $\lambda=0.154$ nm) at 45 kV and 40 mA on a well ground powder sample in order to confirm the presence of Nb catalyst loading in the cathode host samples.

Raman spectroscopy was also performed to validate the presence of Nb catalyst loading in the cathode host samples. It was performed using a 785 nm wavelength laser and a Princeton Instruments Acton SP2500 spectrometer with a shutter time of 20 s.

SEM and TEM were performed using an Apreo FE-SEM and FEI Tecnai F-20 TEM respectively to assess the surface and internal morphology of TiO $_2$ -supported niobium catalyst or TiO $_2$ -based nanotube. Energy dispersive X-ray spectroscopy (EDS) was also performed to validate the presence and distribution of Nb catalyst loading on the surface of TiO $_2$ -based nanotube. It was performed using an Ametek Octane Elite EDS fitted to an Apreo FE-SEM.

3. Results and discussion

3.1. Characterization before cycling

To determine the crystallographic phases of the samples, X-ray diffraction (XRD) pattern investigations on TiO_2 -supported niobium catalyst and TiO_2 -based nanotube were conducted. Fig. S1 (a) shows a comparison of TiO_2 -supported niobium catalyst and TiO_2 -based nanotube, however no significant difference can be asertained between the two. This means that no new phase is formed after Nb doping. This also suggests that Raman spectroscopy is unable to detect the presence of Nb in the samples, indicating that the Nb particles are too small to be resolved by Raman spectroscopy to collect data. In order to validate the presence of Nb catalyst doping within the doped samples, analysis using a technique with a smaller wavelength is necesseatated.

As shown in Fig. S1 (b-c), XRD analysis reveals the presence of several dominant phases present in the heat-treated materials. As shown in Fig. S1 (b), the heat-treated TiO₂-based nanotube shows the presence of rutile TiO₂ and sodium titanium oxide. The presence of sodium in the sample is a result of the synthesis method of the nanostructure, as sodium ions are trapped in the polar TiO₂-based nanotube as they form [31]. Contrasting Fig. S1 (b) with Fig. S1 (c) reveals the presence of several peaks suggesting the presence of Nb catalyst loading in the sample, particularly the (110) peak present at 38.7° . This peak can be identified in the Nb doped sample and not the undoped sample. Unfortunately, many peaks within the samples cannot be identified. This is likely a result of the formation of a large number of minor phases comprised of titanium, oxygen, niobium and sodium which have formed as a result of the large number of chemical and heat treatments [32].

Additional analysis must be performed to fully understand the composition of these samples and confirm the presence of Nb catalyst loading. While the X-rays used to generate data in XRD have an adequately small wavelength to interact with and indicate the presence of Nb catalyst loading, this technique generates too much data about the material, making it difficult to extract meaningful data regarding the distribution and composition of Nb catalyst loading on the surface of the nanostructures.

To determine the composition and identify the chemical states of ${\rm TiO_2}$ -based nanotube and ${\rm TiO_2}$ -supported niobium catalyst, XPS analysis was carried out. As shown in Fig. 1 (a-b), the XPS survey spectra exhibit that ${\rm TiO_2}$ -based nanotube and ${\rm TiO_2}$ -supported niobium catalyst both contain Ti, O, and Na. Additionally, ${\rm TiO_2}$ -supported niobium catalyst shows the existence of Nb element, which confirms the successful loading of Nb catalyst [33–35]. Fig. 1 (c-f) shows Ti 2p and O 1s regions of the high resolution XPS spectra of ${\rm TiO_2}$ -based nanotube and ${\rm TiO_2}$ -supported niobium catalyst. The two noticeable peaks from ${\rm TiO_2}$ -based nanotube and ${\rm TiO_2}$ -supported niobium catalyst at around 465.3 eV and 459.5 eV with symmetry can be attributed to ${\rm Ti}$ 2p1/2 and ${\rm Ti}$ 2p3/2, respectively [36]. The peak positions and 5.8 eV peak separation of the ${\rm Ti}$ 2p doublet agree well with the energy reported for ${\rm TiO_2}$ nanoparticles

[36,37]. The peaks of O 1s are located at about 531.0 eV, whose energy is equal to the O 1s electron binding energy for TiO₂ [38]. Also, there is one more peak in both samples observed at binding energy of 532.0 eV, corresponding to the H–O from the absorbed H₂O on their surface [39]. As shown in Fig. 1(g–h), the extreme resolution Na 1s peak showed a major peak at 1072.0 eV for TiO₂-based nanotube and TiO₂-supported niobium catalyst [40–42]. As shown in Fig. 1 (i), the high resolution Nb 3d displays two noticeable peaks for TiO₂-supported niobium catalyst, confirming the successful loading of Nb catalyst. The peak of Nb 3d_{5/2} is located at 206.3 eV, and the peak of Nb 3d_{3/2} is located at 209.1 eV [43–45].

Fig. 2 (a-b) shows SEM images of each of the cathode host materials for comparison. The TiO_2 -based nanotube and TiO_2 -supported niobium catalyst sample demonstrate a uniform geometry, demonstrating longer and finer granules with less agglomeration and fusing of particles. Additionally, contrasting Fig. 2 (a-b) reveals that the presence of Nb catalyst loading has no impact on the final morphology of the material after heat treatment [46–48].

As shown in Fig. 2 (c-d) and Table 1, the presence and quantity of Nb catalyst loading present in the sample can easily be observed using EDS. The electron beam used by the SEM to generate characteristic X-rays is

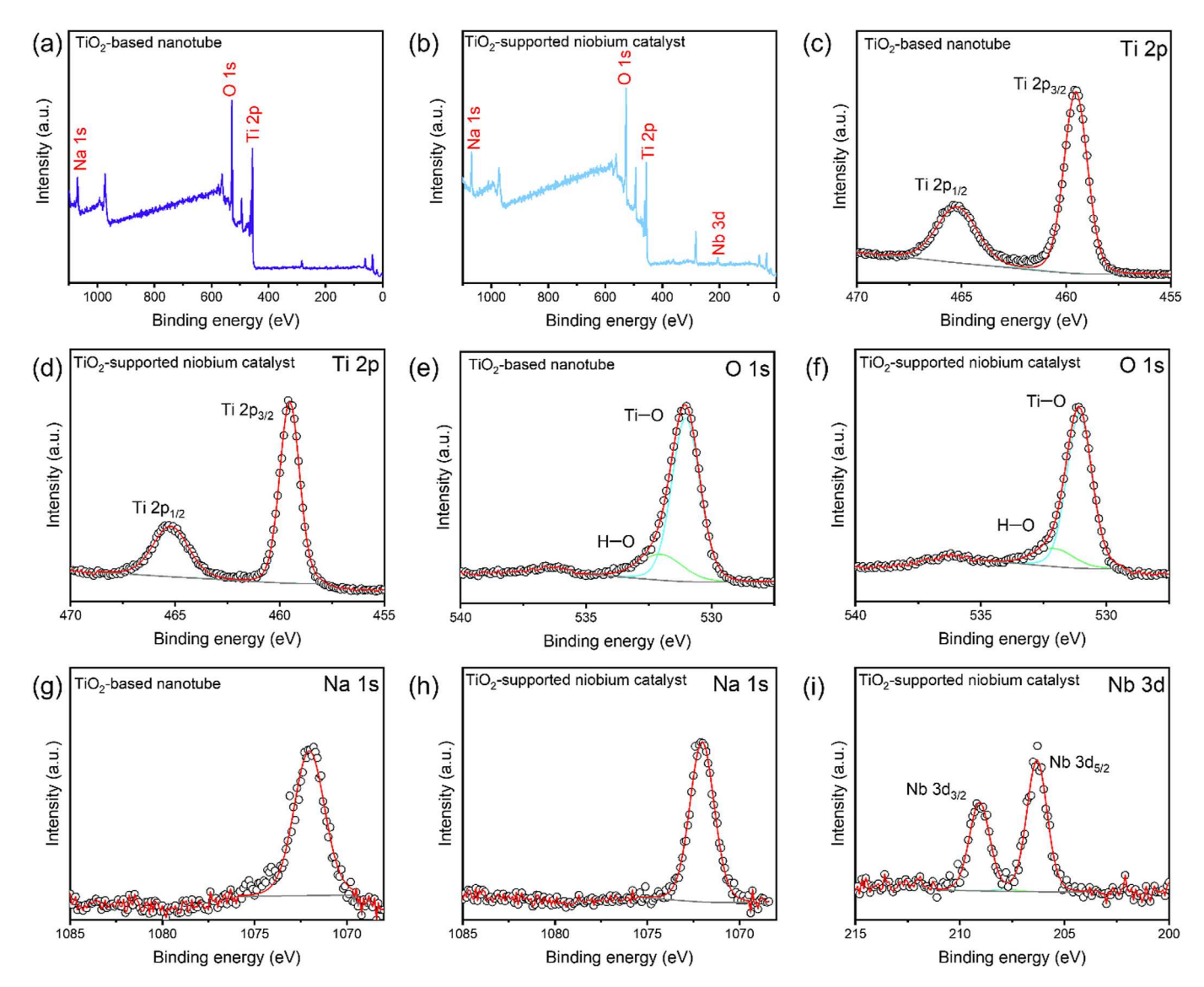


Fig. 1. XPS survey spectra of (a) TiO₂-based nanotube and (b) TiO₂-supported niobium catalyst; Ti 2p high-resolution XPS spectra of (c) TiO₂-based nanotube and (d) TiO₂-supported niobium catalyst; O 1s high-resolution XPS spectra of (e) TiO₂-based nanotube and (f) TiO₂-supported niobium catalyst; Na 1s high-resolution XPS spectra of (g) TiO₂-based nanotube and (h) TiO₂-supported niobium catalyst; Nb 3d high-resolution XPS spectra of (i) TiO₂-supported niobium catalyst.

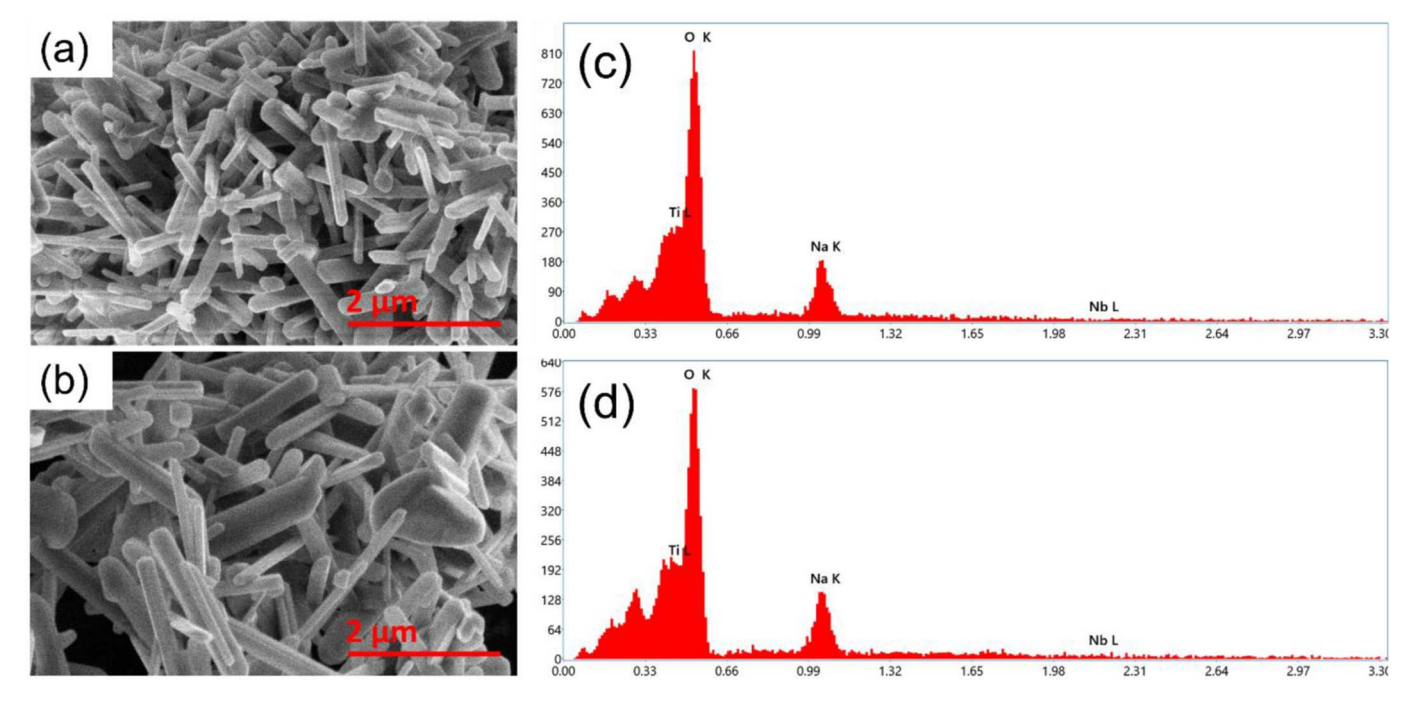


Fig. 2. SEM images taken at 20,000× magnification of (a) TiO₂-based nanotube, and (b) TiO₂-supported niobium catalyst. EDS analysis of (c) TiO₂-based nanotube, and (d) TiO₂-supported niobium catalyst.

small enough to interact with the Nb catalyst, indicating their presence and concentration on the surface of the TiO_2 -based nanotube. Per Table 1, TiO_2 -supported niobium catalyst demonstrated the presence of Nb. As shown in Fig. 2, the size and morphology of TiO_2 -supported niobium catalyst changed a little due to the Nb addition and the thermal treatment. Additionally, SEM imaging and EDS elemental mapping (Fig. S2 (a-f)) of TiO_2 -supported niobium catalyst were carried out, which clearly demonstrate the homogenous distribution of Nb on the TiO_2 -based nanotube.

To substantiate the presence of hollow nanotubes in the TiO2-based nanotube sample, TEM imaging was carried out (Fig. 3 (a-b)). Firstly, a regular TEM image (Fig. 3 (a)) was obtained to show the interior structure of the nanostructures. As shown in Fig. 3 (a), the TiO₂-based nanotube demonstrates an ordered nanorod structure. The lack of contrast in the middle of the sample indicates that the sample possesses a nanotube structure. As TEM displays the "shadow" of matter, the darker portions correspond to be the thicker portions (mass-thickness contrast mechanism), and thus can be interpreted as the walls of a hollow structure. High-resolution TEM image (Fig. 3 (b)) was obtained to estimate an average tube diameter of the TiO2-based nanotube. Analysis from the various locations on the structure yielded an average of about 10.2 nm, with values being clustered between 9 nm and 12 nm. The length could not be determined for the TiO2-based nanotube, as the structures had to be pulverized and ultrasonicated in order to disperse them thinly enough to analyze single structures via TEM.

 $\label{total composition data for samples of TiO_2-based nanotube, TiO_2-supported niobium catalyst obtained via EDS analysis.$

| | Atomic % Ti | Atomic % O | Atomic % Na | Atomic % Nb |
|---|----------------|---------------|----------------|----------------|
| TiO ₂ -based nanotube | 25.08 | 64.35 | 10.51 | _ |
| TiO ₂ -supported niobium catalyst | 25.31 | 62.56 | 11.72 | 0.40 |

3.2. Electrochemical characterization

The electrochemical performance of each cell was validated via EIS, as shown in Fig. 4 (a-d). Potentiostatic EIS testing was performed using CR-2032 type coin cell batteries employing the TiO₂-based nanotube and TiO2-supported niobium catalyst with a frequency window of 0.01–10⁵ Hz. The results of the EIS tests are shown as Nyquist plots (Fig. 4 (a-b)), which graph Z_{real} (denoted Z') against -Z_{imaginary} (denoted Z"). Analyzing the inflection point of these graphs allows values for electrolyte resistance, solid electrolyte interface resistance, and charge transfer resistance to be obtained, denoted Rs, Rf, and Rct respectively [49-52]. As shown in Fig. 4 (a), both cathode host types demonstrated roughly similar values for R_s, due to the fact that each cell shared the electrolyte and the fact that the only variable in the construction of each cell was what host material was loaded onto the carbon cloth electrode. Before cycling (Fig. 4 (a)), the solid electrolyte interface resistance (R_f) and the charge transfer resistance (Rct) value of the TiO2-supported niobium catalyst cell (8.2 Ω and 3.5 Ω respectively) are much smaller than those of the TiO2-based nanotube cell (33.4 Ω and 11.1 Ω respectively), implying an accelerated charge transfer and a promoted redox reaction. After 350 galvanostatic cycles at 3C (Fig. 4 (b)), the high-frequency semicircles of both cells clearly are smaller than those of the fresh cells, implying accelerated charge transport, successful rearrangement of the active material, and more complete electrolyte infiltration after the initial galvanostatic cycles [53]. Elaborately designed TiO₂-supported niobium catalyst cell still exhibited a lower charge transfer resistance representing a significantly smoother charge transfer compared with the TiO₂-based nanotube cell, resulting in faster redox kinetics throughout the entire electrode. Additionally, the lower interface resistivity of the TiO2-supported niobium catalyst sample when compared to the TiO2-based nanotube sample indicates that the presence of Nb catalyst loading has a positive effect on the surface interactions of the materials, with the Nb catalyst loading boosting the electrical conductivity of the sample and thus the rate of the reaction.

Fig. 5 (a) shows the CV data for the TiO_2 -based nanotube and TiO_2 -supported niobium catalyst cells. Measurements were taken with a potential window of 1.7–2.8 V with a scan rate of 0.1 mV s⁻¹. The TiO_2 -supported niobium catalyst sample outperformed the TiO_2 -based

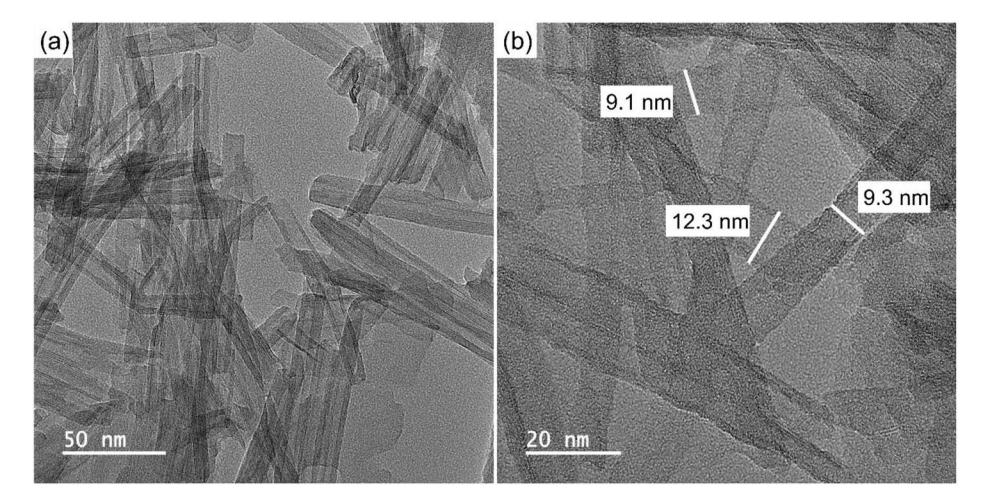


Fig. 3. TEM images of TiO2-based nanotube.

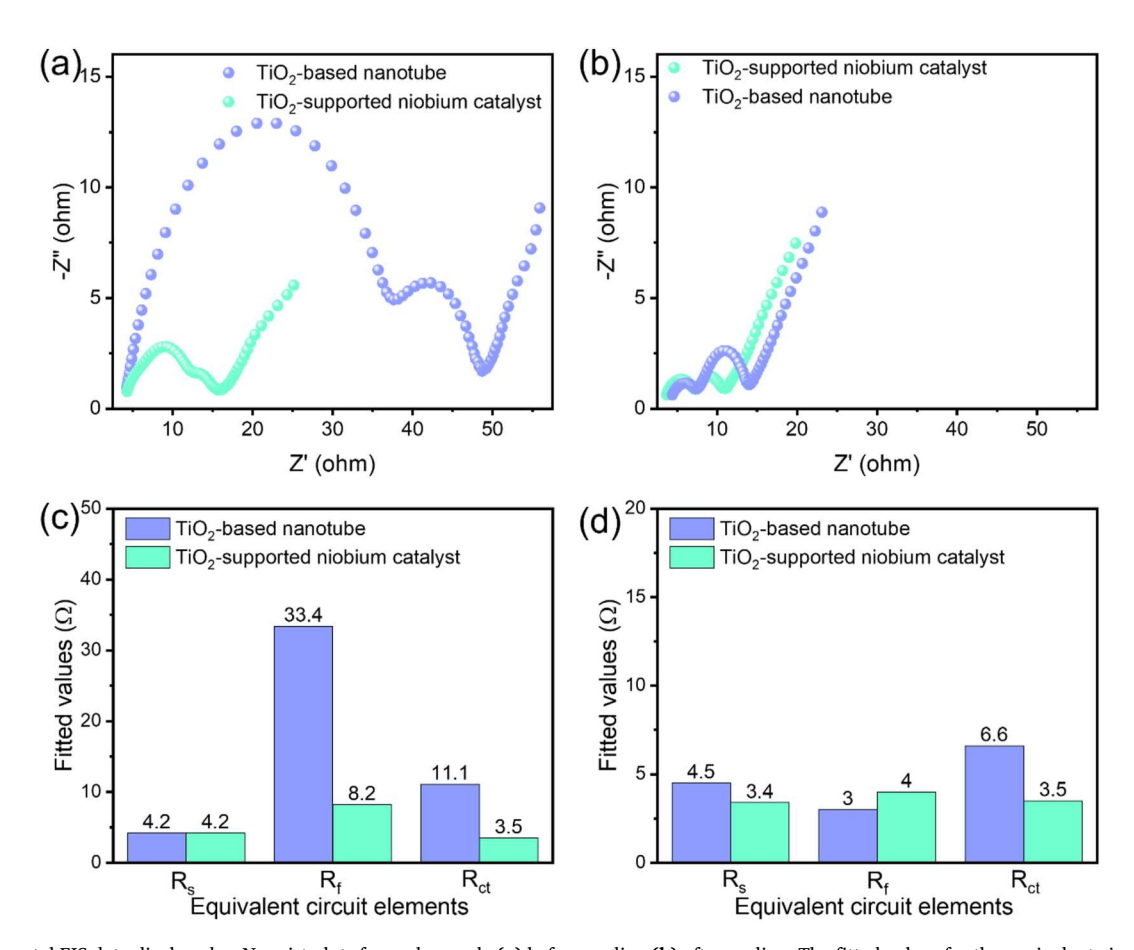


Fig. 4. Experimental EIS data displayed as Nyquist plots for each sample (a) before cycling (b) after cycling. The fitted values for the equivalent circuit elements (c) before cycling and (d) after cycling.

nanotube sample in terms of the measured current rate at the anodic and cathodic peaks (Fig. 5 (b)), indicating superior electron transfer performance. This implies that the TiO_2 -supported niobium catalyst sample had a superior conductivity, which echoes the low R_{ct} value obtained in the EIS testing. These results also indicate that the TiO_2 -supported niobium catalyst sample allowed a higher rate of charge transfer, as more lithium polysulfides were able to interact with the surface of the cathode host simultaneously. The Tafel plots are deduced from the potentiostatic polarization experiments at the CV peak position, and they can reflect the kinetic behavior of electrochemical process. It is

apparent that the TiO_2 -supported niobium catalyst cell demonstrates a higher onset potential for the electrochemical reduction of polysulfides than the TiO_2 -based nanotube cell (Fig. 5 (c) and (e)), suggesting a lower energy barrier for polysulfide catalytic conversion. Additionally, the TiO_2 -supported niobium catalyst cell also exhibits a lower onset potential as well as a higher current response for the Li_2S oxidation to the soluble long-chain polysulfides than the TiO_2 -based nanotube cell (Fig. 5 (g)), implying a lower energy barrier for Li_2S decomposition [54]. Further investigation of the electrocatalytic effect was carried out by comparing the slopes of the fitted Tafel plots. The TiO_2 -supported

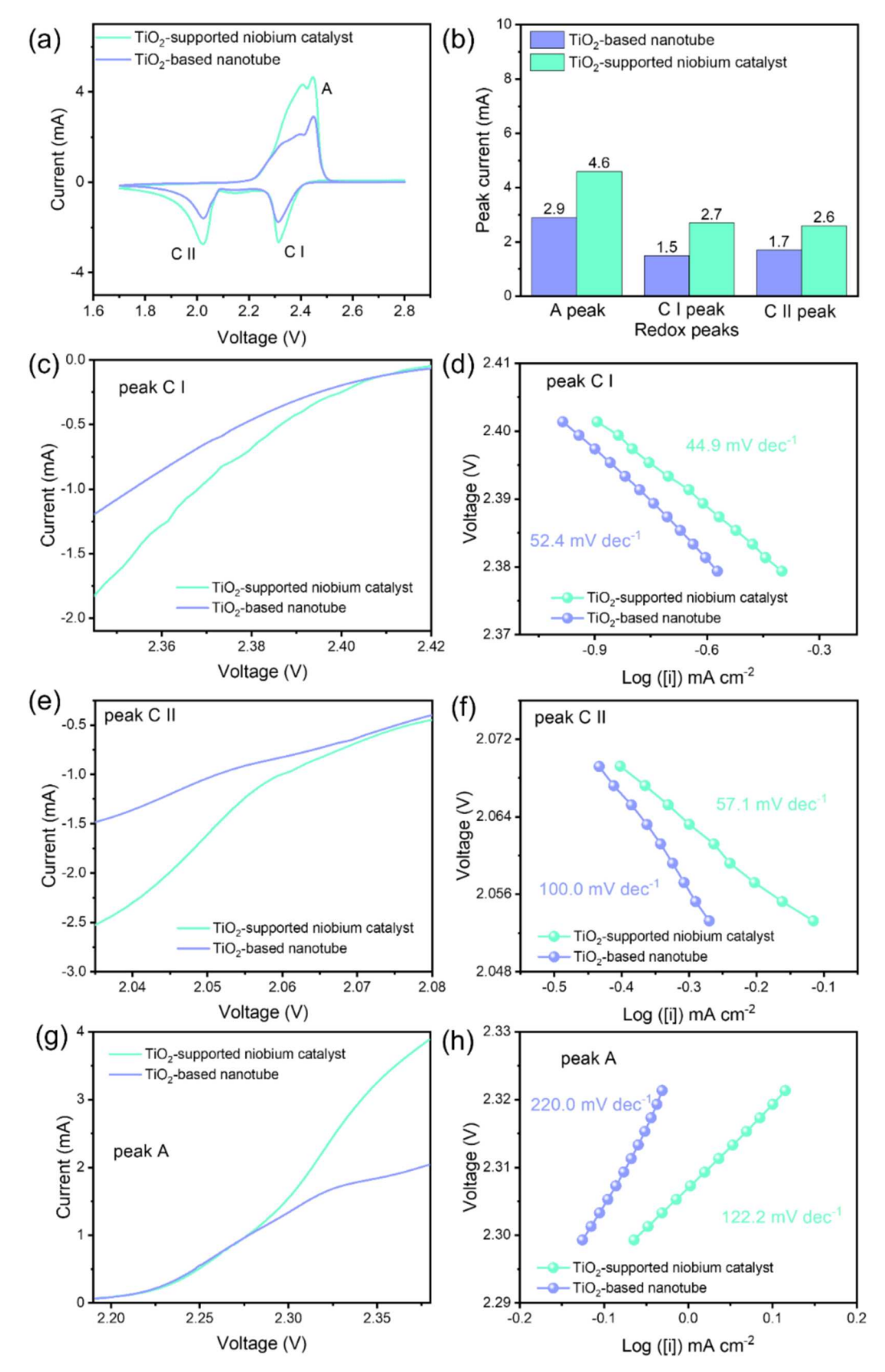


Fig. 5. (a) Experimental CV data, and (b) peak current comparison about each redox peak of the TiO₂-based nanotube cell and the TiO₂-supported niobium catalyst cell. (c) Potentiostatic polarization curves, and (d) corresponding Tafel plots of the peak C I; (e) Potentiostatic polarization curves, and (f) corresponding Tafel plots of the peak C II; (g) Potentiostatic polarization curves, and (h) corresponding Tafel plots of the peak A.

niobium catalyst cell demonstrates a smaller slope during both the reduction (Fig. 5 (d) and (f)) and oxidation processes (Fig. 5 (h)). For instance, the TiO $_2$ -supported niobium catalyst cell exhibits a lower Tafel slope (44.9 mV dec $^{-1}$ for peak C I, 57.1 mV dec $^{-1}$ for peak C II, and 122.2 mV dec $^{-1}$ for peak A) compared to those of the TiO $_2$ -based nanotube cell (52.4 mV dec $^{-1}$ for peak C I, 100.0 mV dec $^{-1}$ for peak C II, and 220.0 mV dec $^{-1}$ for peak A). The noticeable decrease in the Tafel slope values substantiates the increased rate of polysulfide redox conversion [55–57].

To understand the catalytic effect of TiO2-supported niobium catalyst additive on the sulfur species redox chemistry, CV in the symmetric cells which comprise two identical TiO2-based nanotube or TiO2-supported niobium catalyst as both working and counter electrodes was measured (Fig. 6). Interestingly, three pairs of reversible redox peaks are observed in the CV curve of the TiO₂-supported niobium catalyst cell (Fig. 6 (a)). These peaks exhibit sharpness or narrow shape for each redox pair, suggesting excellent catalytic activity and kinetics characteristics for LiPSs conversion [58]. However, only two pairs of peaks are found in the CV curve of the TiO2-based nanotube cell, which are assigned as the decomposition of S₈ to Li₂S₄ (peak A) and the electrochemical reduction of Li₂S₄ to Li₂S (peak C), respectively [59]. The corresponding electrochemical reactions for those redox peaks of the TiO2-based nanotube cell or TiO2-supported niobium catalyst cell are summarized in Fig. 6 (b). Each peak corresponds to a specific chemical redox reaction during cycling. It is worth noting that the peak pairs (a/A, c/C, a'/A', and c'/C') show a very similar voltage position. Therefore, as shown in Fig. 6(b), these peak pairs are assigned as the same electrochemical redox reactions. Based on the voltage position of the b/b' redox peak pair, the corresponding chemical reactions are associated with the electrochemical reduction from long-chain Li₂S₈ to Li₂S₄ and the electrochemical oxidation from Li₂S₄ to soluble high-order Li₂S₈, respectively. The appearance of the b/b' redox peak pair confirms the favorable catalytic effect of the TiO_2 -supported niobium catalyst electrode on the electrochemical conversion between a large number of high-order Li_2S_8 and low-order Li_2S_4 [59]. The integration of the CV profiles also indicates that the TiO_2 -supported niobium catalyst cell presents rapid diffusion and transfer of electrons/ions due to the catalytic effect of niobium on the polysulfide conversion. Considering the roles of polar TiO_2 support and niobium catalyst, the TiO_2 -supported niobium catalyst combines the advantages of strong anchoring for LiPSs with good nucleation/decomposition of Li_2S and surface diffusion for accelerating bidirectional sulfur redox kinetics (both the reduction of LiPSs and the oxidation of insoluble Li_2S/Li_2S_2), thereby to achieve the balanced adsorption-catalytic conversion-nucleation behaviors for sulfur species and alleviate the polysulfide shuttle effect, and finally leading to outstanding electrochemical performance (Fig. 6 (c)).

The nucleation and dissolution of Li₂S were carried out to demonstrate the improved redox reactions with the help of TiO₂-supported niobium catalyst. The nucleation experiments (Fig. S3 (a-b)) exhibit the capacity of precipitated Li₂S on TiO₂-supported niobium catalyst (328 mAh g $^{-1}$), which is much higher than that on TiO₂-based nanotube (155 mAh g $^{-1}$). To evaluate the dissolution behaviors of Li₂S on TiO₂-supported niobium catalyst and TiO₂-based nanotube surface, the potentiostatic charge experiments were implemented at 2.38 V (Fig. S3 (c-d)). TiO₂-supported niobium catalyst exhibits a higher capacity (387 mAh g $^{-1}$) for Li₂S dissolution compared to the TiO₂-based nanotube (216 mAh g $^{-1}$). These results verified the bidirectional roles of TiO₂-supported niobium catalyst in the redox conversion between LiPSs and Li₂S.

To investigate the influence of loading Nb catalyst in TiO_2 -based nanotube on electrochemical performance, the coin-type cells were fabricated with TiO_2 -supported niobium catalyst and TiO_2 -based nanotube. The maximum initial specific capacity and overall stability of each sample were assessed via a "steps" test in which the C rate was changed every 5 cycles as follows: 0.2, 0.5, 1.0, 2.0, 3.0, 2.0, 1.0, 0.5, 0.2 C. The

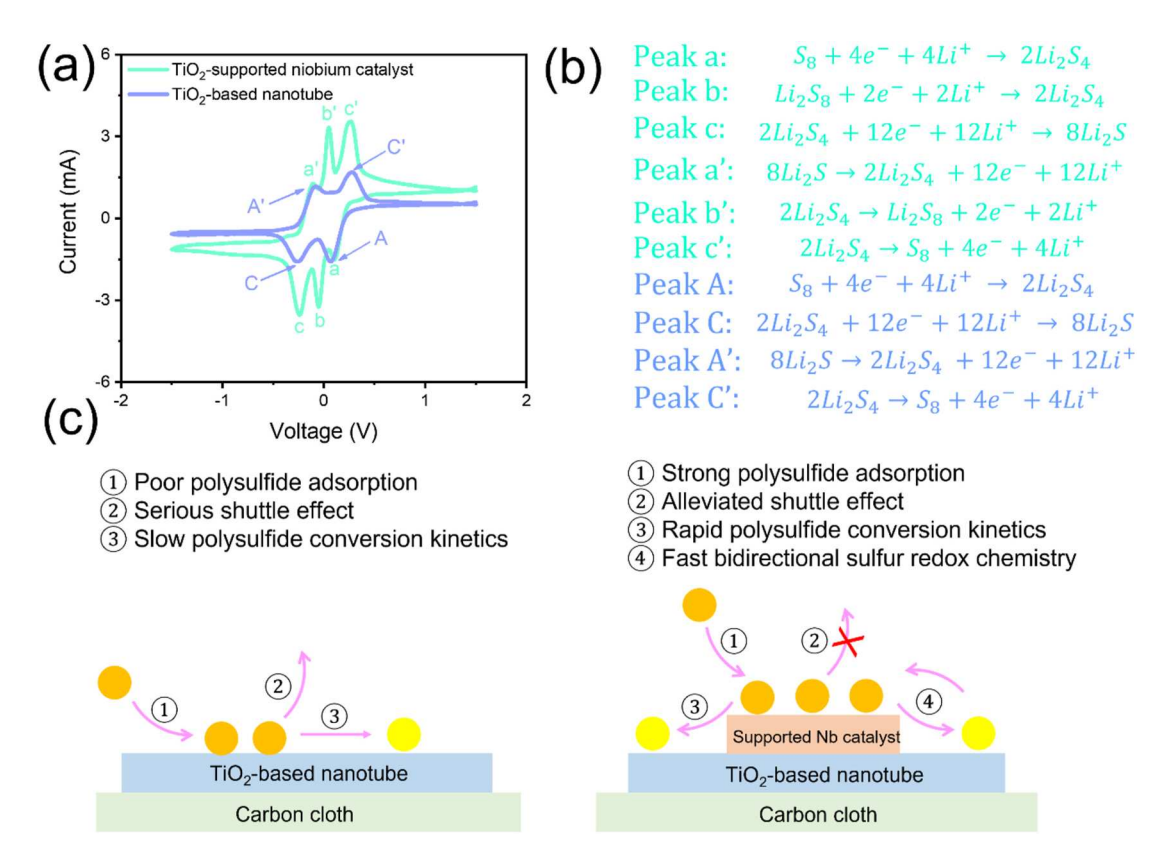


Fig. 6. (a) The CV profiles of the symmetric cells based on TiO₂-based nanotube and TiO₂-supported niobium catalyst; (b) The corresponding chemical reactions for the redox peaks in (a) of the TiO₂-based nanotube and TiO₂-supported niobium catalyst cells; (c) The working mechanism comparison for the TiO₂-based nanotube and TiO₂-supported niobium catalyst cells.

results of this test are shown in Fig. 7 (a-d). The cells exhibit two voltage plateaus at the discharge curves and one voltage plateau at the charge curves. During discharge, the first plateau corresponds to the electrochemical transition from solid S₈ to soluble LiPS, and the second plateau corresponds to the electrochemical transition from liquid LiPS to solid Li₂S₂/Li₂S. During charge process, the plateau is ascribed to the conversion of Li₂S₂/Li₂S to S₈ [60,61]. The charge-discharge profiles of the cell with TiO2-supported niobium catalyst display a lower electrochemical polarization at all current densities. These phenomena suggest the improvement of LiPSs conversion kinetics by introducing Nb catalyst into TiO2-based nanotube. Additionally, the cell based on TiO2-supported niobium catalyst delivers a higher average discharge capacity of 961 mAh $\rm g^{-1}, 816$ mAh $\rm g^{-1}, 758$ mAh $\rm g^{-1}, 701$ mAh $\rm g^{-1}$ and 629 mAh g^{-1} at 0.2C, 0.5C, 1C, 2C, and 3C (1C = 1675 mAh g^{-1}), respectively. The cells using the TiO₂-supported niobium catalyst cathode host material outperformed the cells using the TiO2-based nanotube cathode host materials significantly. The cell based on TiO2-based nanotube delivers an average discharge capacity of 713 mAh $\rm g^{-1}$, 605 mAh $\rm g^{-1}$, 537 mAh $\rm g^{-1}$, 479 mAh $\rm g^{-1}$ and 407 mAh $\rm g^{-1}$ at 0.2C, 0.5C, 1C, 2C, and 3C, respectively. Furthermore, the capacity of the cell with TiO2-supported niobium catalyst (Fig. 7 (d)) recovers to 921 mAh g⁻¹ when the current density decreases back to 0.2C, suggesting the outstanding rate performance and superior electrochemical reversibility of the cell with TiO2-supported niobium catalyst. The superior high-rate performance of the TiO₂-supported niobium catalyst sample indicates there is a positive impact on reaction speed from the presence of Nb catalyst loading on the sample, as more of the reduction reaction's electrochemical energy is captured at these high rates [62-64]. The cycle performance of the cells with TiO2-supported niobium catalyst and TiO₂-based nanotube is further evaluated at 3.0 C. As shown in Fig. 7 (e), an initial capacity of 575 mAh g^{-1} can be obtained by the cell with TiO2-supported niobium catalyst at 3.0 C, which is higher than the capacity of the cell with TiO_2 -based nanotube (461 mAh g^{-1}). After 350 cycles, a retainable capacity of 484 mAh $\rm g^{-1}$ can be obtained by the cell with TiO₂-supported niobium catalyst. As a contrast, the capacity of the cell with TiO₂-based nanotube could only maintain 443 mAh g⁻¹ after 350 cycles. The defect design endows the TiO₂-supported niobium catalyst cell with significantly enhanced electron conductivity and stronger chemical adsorption toward polysulfide [65-67]. The cycling performances of the TiO2-supported niobium catalyst and TiO2-based nanotube cells at 0.2 C over 100 cycles are presented in Fig. 7 (f). The TiO₂-supported niobium catalyst cell exhibits a higher initial capacity of 966 mAh g^{-1} than that of the TiO₂-based nanotube cell (721 mAh g^{-1}). The TiO2-supported niobium catalyst electrode can still deliver a reversible capacity of 947 mAh g^{-1} even after 100 cycles, which is superior to the electrode (657 mAh g^{-1}). Since the TiO₂-supported niobium catalyst electrode demonstrated a more favorable electrochemical performance under low sulfur loading than the TiO2-based nanotube sample, furthermore, taking the practical commercialization into account, the electrochemical measurement with high areal sulfur loading (5 mg cm⁻²) was carried out. Fig. 7 (g) exhibits during 100 cycles at 0.1 C, the initial capacity of the TiO2-supported niobium catalyst cell was 777 mAh g⁻¹ under a high areal sulfur loading of 5 mg cm $^{-2}$, while the TiO₂-based nanotube sample was only 632 mAh g $^{-1}$. This shows that the TiO₂-supported niobium catalyst cell could still have a good performance even with a high areal sulfur loading of 5 mg cm⁻² prone to shuttle effect. As shown in the long cycle at 0.1 C in Fig. 7 (g), the capacity of the TiO2-supported niobium catalyst cell was still maintained at 744 mAh $\rm g^{-1}$ at 100th cycle, higher than that of the $\rm TiO_2$ -based nanotube cell (568 mAh $\rm g^{-1}$ at 100th cycle), and it achieved a comparably small capacity decay rate (0.042 % per cycle).

The best rate performance was observed for the TiO_2 -supported niobium catalyst cathode host material, demonstrating an initial capacity of 961 mAh g⁻¹ at 0.2 C and 629 mAh g⁻¹ at 3.0 C. The superior high-rate performance of the TiO_2 -supported niobium catalyst sample to the TiO_2 -based nanotube sample can be attributed to the presence of Nb

catalyst loading, as their catalytic effect allows for enhanced Li–S reduction kinetics at higher rates, enabling higher useable specific capacities to be achieved.

 ${
m TiO_2}$ -supported niobium catalyst cathode host materials also demonstrated excellent stability over extended cycling, with a decay rate of 0.045 % per cycle over the 350 cycles. This decay rate indicates that there is no "tipping point" for capacity retention for the ${
m TiO_2}$ -supported niobium catalyst cathode host material, indicating a very high level of stability. These results indicate that the higher surface area demonstrated by the more ordered, less agglomerated ${
m TiO_2}$ -based nanotube materials led to a higher cycle life, and that the presence of Nb catalyst loading allowed the ${
m TiO_2}$ -supported niobium catalyst cathode host sample to demonstrate excellent stability and high-capacity retention.

The LiPSs shuttling causes the active materials in the cathode to become unstable during the multi-step redox reactions undergone during charge and discharge cycling. This instability allows the active materials to detach from the cathode host, dissolving into the electrolyte in the form of soluble LiPSs. This phenomenon causes the viscosity of the electrolyte to increase and leads to self-discharging, the combination of which results in significant capacity loss and a low Coulombic efficiency. The self-discharging caused in the cell by the dissolution of LiPSs into the electrolyte is one of the greatest technical barriers to commercialization of this technology.

A self-discharge test was carried out to evaluate the LiPSs adsorption of the TiO₂-supported niobium catalyst cell and the TiO₂-based nanotube cell. Firstly, both coin cells were galvanostatically cycled at 0.2 C for 10 cycles. Then, the cells were rested for 24 h before the 11th cycle at 0.2 C. Severe self-discharge behavior can be observed from the TiO₂-based nanotube cell. As shown in Fig. S4, the TiO₂-based nanotube cell experienced a serious irreversible capacity loss of 17.4 % after 24 h of rest. In contrast, the TiO₂-supported niobium catalyst cell demonstrated a capacity loss of only 6.1 % after resting for 24 h, which confirms that self-discharge behavior was significantly mitigated. This indicates that the TiO₂-supported niobium catalyst contributes to the anti-self-discharge feature.

After 100 cycles at 0.2 C, the TiO₂-supported niobium catalyst cell and the TiO2-based nanotube cell were disassembled inside the glovebox, and the separators and Li anodes were collected. The visual observation of the cycled separators can be achieved from Fig. 8 (a-b). The separator from the TiO₂-supported niobium catalyst cell was clean and fresh suggesting minimal polysulfide migration and effective immobilization of polysulfides by TiO₂-supported niobium catalyst. However, the heavily yellow-colored separator from the TiO2-based nanotube cell exhibited severe polysulfide shuttling issue, leading to a huge loss of active material. Additionally, the Li metal anode in the TiO2supported niobium catalyst cell shows a cleaner surface without noticeable corrosion (Fig. 8 (c)). Yellow substances were observed on the surface of the cycled Li anode in the TiO₂-based nanotube cell (Fig. 8 (d)), implying the serious shuttling issue. The TiO₂-based nanotube can only address the shuttle effect issue to some extent. For the TiO₂-based nanotube during long-term cycling, a great amount of active material was lost due to the insufficient restriction and sluggish conversion of polysulfides.

A credible confirmation in support of alleviated polysulfide migration was made by observing the surface of the cycled Li metal anode [68–70]. The TiO_2 -supported niobium catalyst cell and the TiO_2 -based nanotube cell were dissembled inside of Argon-filled glovebox after cycling. As demonstrated in Fig. 9 (a), a smooth surface without obvious pulverization or cracks was observed from the TiO_2 -supported niobium catalyst cell, suggesting that polysulfides are effectively trapped on the cathode side through the strong chemical bonding with the TiO_2 -supported niobium catalyst. As shown in Fig. 9 (c), numerous cracks and a large amount of $\text{Li}_2\text{S}_2/\text{Li}_2\text{S}$ deposition were easily observed from the TiO_2 -based nanotube cell. The shuttle effect can be mitigated to some extent by using the TiO_2 -based nanotube. However, the TiO_2 -based

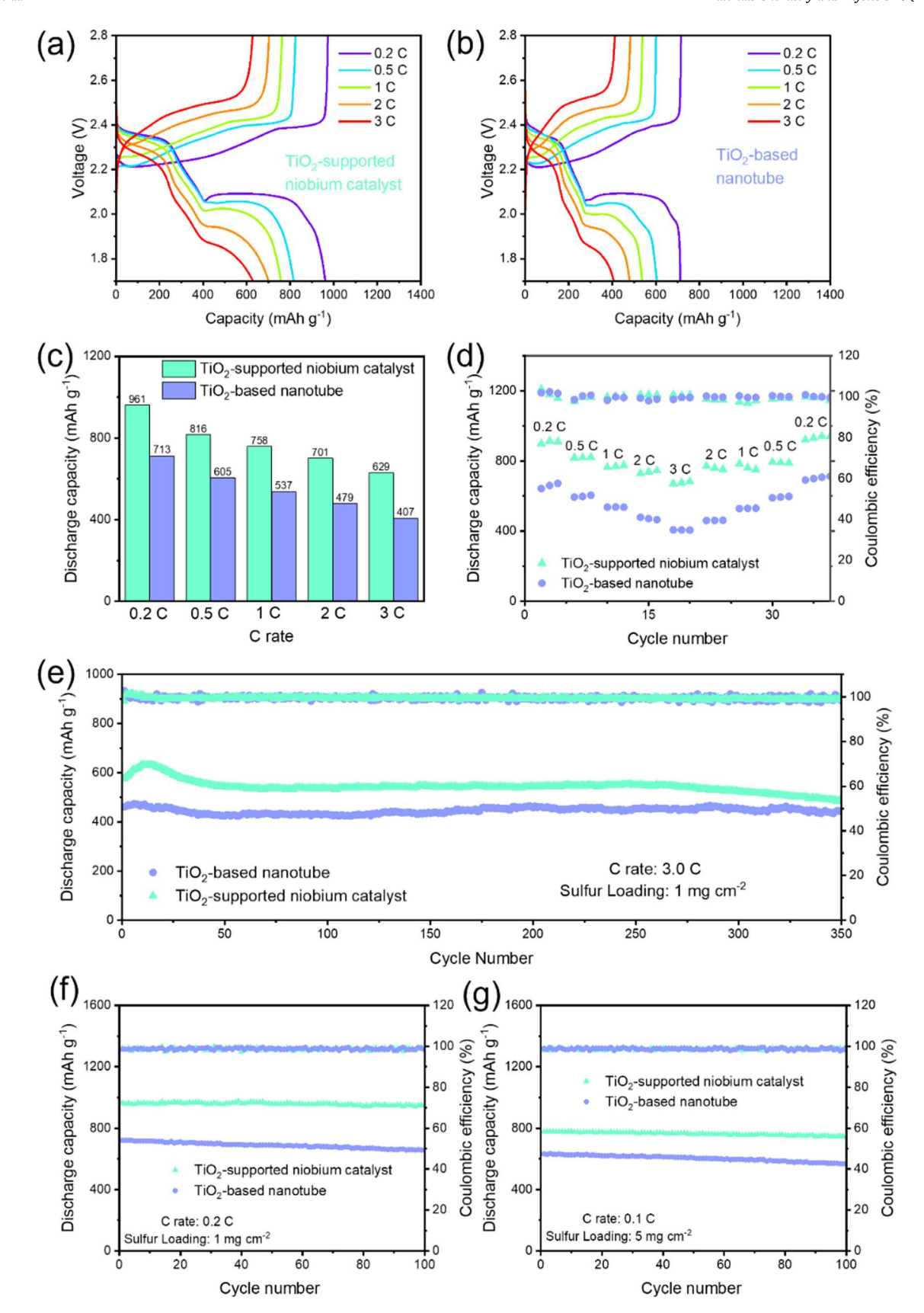


Fig. 7. (a–b) Charge-discharge cycling profiles of Li–S batteries at various charge rates using TiO₂-based nanotube and TiO₂-supported niobium catalyst materials respectively. (c) the comparison of specific discharge capacities at various current rates (d) displays of "steps" tests conducted on Li–S batteries between charge rates of 0.2 and 3.0 C for TiO₂-based nanotube and TiO₂-supported niobium catalyst. (e) display long cycling tests conducted at 3.0 C, showing the first 350 cycles. (f) Cycling performance of the TiO₂-based nanotube cell and the TiO₂-supported niobium catalyst cell at 0.2 C for 100 cycles. (g) Cycling performance of the TiO₂-based nanotube cell with high sulfur loading (5 mg cm⁻²) at 0.1 C for 100 cycles.

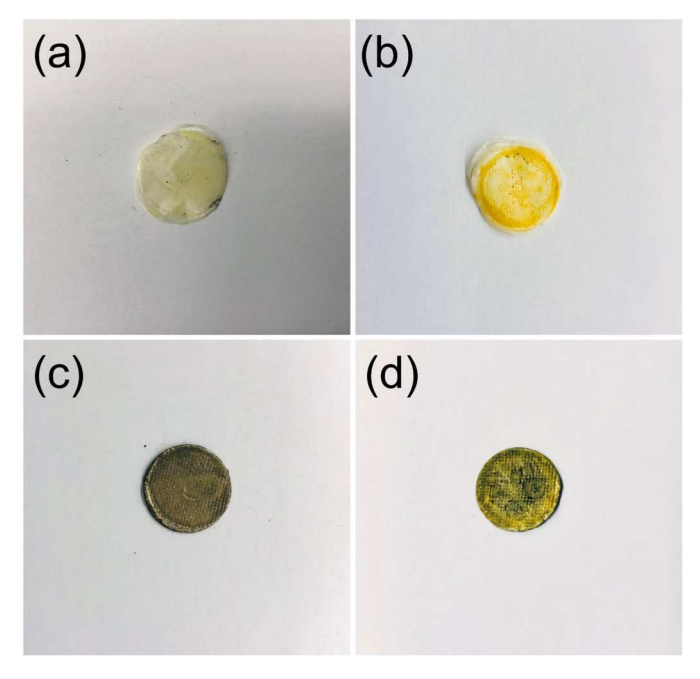


Fig. 8. The optical photos of (a) the cycled separator and (c) the cycled Li anode from the ${\rm TiO_2}$ -supported niobium catalyst cell; The optical photos of (b) the cycled separator and (d) the cycled Li anode from the ${\rm TiO_2}$ -based nanotube cell.

nanotube was not capable of successfully immobilizing polysulfide species during long-term cycling due to the limited adsorption capability and the poor electronic conductivity. Moreover, the EDS elemental mapping of Li anode with TiO_2 -supported niobium catalyst shows a much less deposition of sulfur element than the one with TiO_2 -based

nanotube (Fig. 9 (b) and (d)).

4. Conclusion

TiO2-based nanotubes with an intrinsic polar nature and high phase stability are a promising host for Nb catalyst loading. Additionally, niobium and titanium have the similar ionic size, leading to easy infiltration of the niobium catalyst into the TiO₂ crystal lattice, significantly increasing the presence of conductive titanium ions and further improving the material's electrical conductivity. The rich defects of the TiO₂-supported niobium catalyst offer a huge number of catalytic sites that can chemically adsorb the polysulfides and simultaneously accelerate their conversion reactions. The effectiveness of the Nb catalyst loading hosted on TiO2 based nanostructures as a host and catalyst material for Li-S batteries can be attributed to its ability to infiltrate the lattice of TiO₂ based crystals and increase the concentration of Ti³⁺ ions due to their similar atomic size and mismatched valance state. Testing showed that in refined TiO2 materials, such as TiO2-supported Nb, catalyst loading resulted in lower charge transfer resistances than the TiO₂-based nanotube alone. The Nb catalyst loading also enabled higher capacity retention at high rates for the TiO₂-supported niobium catalyst sample over the TiO2-based nanotube sample while retaining similar long term cycling performance and stability.

Overall, the presence of Nb catalyst loading on TiO₂-based nanotube host materials allowed for effective alleviation of polysulfide diffusion and extremely stable cell performance for over 350 cycles. The contribution of the Nb catalyst loading to performance was validated through comparison to identical materials without Nb loading, which demonstrated inferior performance at high charge rates. The proposed working mechanism for this phenomenon is that the high surface area polar TiO₂-based nanotube material is able to chemically retain LiPS, and Nb catalyst loading on the surface of the material are able to improve polarity and reduction kinetics to prevent capacity fading. This work demonstrates a synergistic effect of defect fabrication and structural

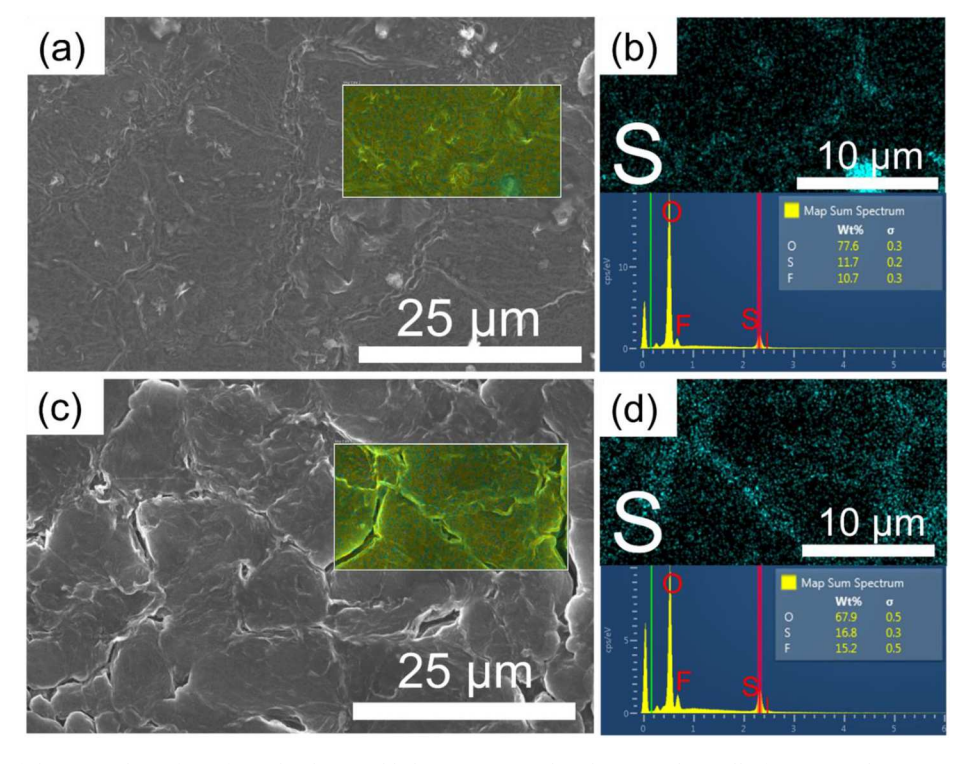


Fig. 9. (a) SEM images of the Li anode surfaces from the disassembled TiO₂-supported niobium catalyst cell after 100 cycles at 0.2 C; (b) Corresponding EDS elemental mapping of the Li anode surfaces from the TiO₂-supported niobium catalyst cell after 100 cycles at 0.2 C; (c) SEM images of the Li anode surfaces from the disassembled TiO₂-based nanotube cell after 100 cycles at 0.2 C; (d) Corresponding EDS elemental mapping of the Li anode surfaces from the TiO₂-based nanotube cell after 100 cycles at 0.2 C.

design that proposes a meaningful attempt toward enhancing the electrochemical performances of Li–S batteries.

CRediT authorship contribution statement

Zephyr Barlow: Investigation, Methodology, Formal analysis, Writing – original draft, Writing – review & editing. **Zhen Wei:** Investigation, Methodology, Formal analysis, Writing – review & editing. **Ruigang Wang:** Conceptualization, Supervision, Writing – review & editing, Funding acquisition.

Declaration of competing interest

The authors declare that they have no known competing financial interests or personal relationships that could have appeared to influence the work reported in this paper.

Data availability

No data was used for the research described in the article.

Acknowledgment

This work is supported by the National Science Foundation (CBET-2118784 and TI-2147564). This project also receives partial financial support from Alabama Transportation Institute and Alabama Water Institute. The use of electron microscopy facilities at the Alabama Analytical Research Center (AARC), The University of Alabama, is gratefully acknowledged.

Appendix A. Supplementary data

Supplementary data to this article can be found online at $\frac{\text{https:}}{\text{doi.}}$ org/10.1016/j.matchemphys.2023.128830.

References

- M. Zhang, H. Du, Z. Wei, X. Zhang, R. Wang, Ultrafast microwave synthesis of nickel-cobalt sulfide/graphene hybrid electrodes for high-performance asymmetrical supercapacitors, ACS Appl. Energy Mater. 4 (2021) 8262–8274.
- [2] M. Zhang, H. Du, Z. Wei, X. Zhang, R. Wang, Facile electrodeposition of Mn-CoP nanosheets on Ni foam as high-rate and ultrastable electrodes for supercapacitors, ACS Appl. Energy Mater. 5 (2021) 186–195.
- [3] M. Zhang, A. Nautiyal, H. Du, Z. Wei, X. Zhang, R. Wang, Electropolymerization of polyaniline as high-performance binder free electrodes for flexible supercapacitor, Electrochim. Acta 376 (2021), 138037.
- [4] X. Guo, H. Xu, W. Li, Y. Liu, Y. Shi, Q. Li, H. Pang, Embedding atomically dispersed iron sites in nitrogen-doped carbon frameworks-wrapped silicon suboxide for superior lithium storage, Adv. Sci. 10 (2023), 2206084.
- [5] D. Guan, C. Shi, H. Xu, Y. Gu, J. Zhong, Y. Sha, Z. Hu, M. Ni, Z. Shao, Simultaneously mastering operando strain and reconstruction effects via phasesegregation strategy for enhanced oxygen-evolving electrocatalysis, J. Energy Chem. 82 (2023) 572–580.
- [6] S. Urbonaite, T. Poux, P. Novák, Progress towards commercially viable Li–S battery cells, Adv. Energy Mater. 5 (2015), 1500118.
- [7] W. Li, X. Guo, P. Geng, M. Du, Q. Jing, X. Chen, G. Zhang, H. Li, Q. Xu, P. Braunstein, Rational design and general synthesis of multimetallic metal-organic framework nano-octahedra for enhanced Li–S battery, Adv. Mater. 33 (2021), 2105163.
- [8] S. Meini, R. Elazari, A. Rosenman, A. Garsuch, D. Aurbach, The use of redox mediators for enhancing utilization of Li2S cathodes for advanced Li–S battery systems, J. Phys. Chem. Lett. 5 (2014) 915–918.
- [9] Y. Liang, Z. Wei, H.-E. Wang, M. Flores, R. Wang, X. Zhang, Flexible and freestanding PANI: PSS/CNF nanopaper electrodes with enhanced electrochemical performance for supercapacitors, J. Power Sources 548 (2022), 232071.
- [10] Y. Liang, Z. Wei, H.-E. Wang, R. Wang, X. Zhang, Flexible freestanding conductive nanopaper based on PPy: PSS nanocellulose composite for supercapacitors with high performance, Sci. China Mater. (2022) 1–10.
- [11] Y. Liang, Z. Wei, R. Wang, X. Zhang, The microwave facile synthesis of NiOx@ graphene nanocomposites for application in supercapacitors: insights into the formation and storage mechanisms, Coatings 12 (2022) 1060.
- [12] Y. Liang, Z. Wei, X. Zhang, R. Wang, Fabrication of vanadium oxide@ polypyyrole (V2O5@ PPy) core-shell nanofiber electrode for supercapacitor, ES Energy Environment 18 (2022) 101–110.

- [13] B. Zhang, C. Luo, Y. Deng, Z. Huang, G. Zhou, W. Lv, Y.B. He, Y. Wan, F. Kang, Q. H. Yang, Optimized catalytic WS2–WO3 heterostructure design for accelerated polysulfide conversion in lithium–sulfur batteries, Adv. Energy Mater. 10 (2020), 2000091
- [14] Y. Song, H. Li, J. Li, J. An, J.-J. Shao, G. Zhou, Rationalizing the impact of oxygen vacancy on polysulfide conversion kinetics for highly efficient lithium-sulfur batteries, J. Energy Chem. 87 (2023) 51–60.
- [15] Y. Song, S. Zhu, X. Long, Z. Luo, Q. Sun, C. Geng, H. Li, Z. Han, Q. Ouyang, G. Zhou, Mesoporous hydroxyl vanadium oxide/nitrogen-doped graphene enabled fast polysulfide conversion kinetics for high-performance lithium-sulfur batteries, Electrochim. Acta 441 (2023), 141875.
- [16] P. Wang, B. Xi, M. Huang, W. Chen, J. Feng, S. Xiong, Emerging catalysts to promote kinetics of lithium-sulfur batteries, Adv. Energy Mater. 11 (2021).
- [17] Z. Liang, J. Shen, X. Xu, F. Li, J. Liu, B. Yuan, Y. Yu, M. Zhu, Advances in the development of single-atom catalysts for high-energy-density lithium-sulfur batteries, Adv Mater 34 (2022), e2200102.
- [18] Y. Zhang, C. Kang, W. Zhao, Y. Song, J. Zhu, H. Huo, Y. Ma, C. Du, P. Zuo, S. Lou, G. Yin, D-p hybridization-induced "Trapping-Coupling-Conversion" enables high-efficiency Nb single-atom catalysis for Li-S batteries, J. Am. Chem. Soc. 145 (2023) 1728–1739.
- [19] Y. Zhang, L. Guo, L. Tao, Y. Lu, S. Wang, Defect-based single-atom electrocatalysts, Small Methods 3 (2019), 1800406.
- [20] S. Evers, T. Yim, L.F. Nazar, Understanding the nature of absorption/adsorption in nanoporous polysulfide sorbents for the Li–S battery, J. Phys. Chem. C 116 (2012) 19653–19658.
- [21] M. Liu, S. Jhulki, A. Magasinski, P.F. Wang, G. Yushin, Porous TiO(2-x)/C nanofibers with axially aligned tunnel pores as effective sulfur hosts for stabilized lithium-sulfur batteries, ACS Appl. Mater. Interfaces 14 (2022) 54725–54735.
- [22] T. Ji, Z. Li, C. Liu, X. Lu, L. Li, J. Zhu, Niobium-doped TiO2 solid acid catalysts: strengthened interfacial polarization, amplified microwave heating and enhanced energy efficiency of hydroxymethylfurfural production, Appl. Catal. B Environ. 243 (2019) 741–749.
- [23] H. Cai, X. Wu, J. Gao, Effect of oxygen content on structural and transport properties in SrTiO3- x thin films, Chem. Phys. Lett. 467 (2009) 313-317.
- [24] W. Tuichai, S. Danwittayakul, N. Chanlek, P. Thongbai, S. Maensiri, High-performance giant-dielectric properties of rutile TiO2 co-doped with acceptor-Sc3 + and donor-Nb5+ ions, J. Alloys Compd. 703 (2017) 139–147.
- [25] C. Cavallo, G. Calcagno, R.P. de Carvalho, M. Sadd, B. Gonano, C.M. Araujo, A.E. C. Palmqvist, A. Matic, Effect of the niobium doping concentration on the charge storage mechanism of mesoporous anatase beads as an anode for high-rate Li-ion batteries, ACS Appl. Energy Mater. 4 (2020) 215–225.
- [26] H. Bi, S. Zhu, Y. Liang, H. Jiang, Z. Li, S. Wu, H. Wei, C. Chang, H. Wang, Z. Cui, Nb-doped TiO(2) with outstanding Na/Mg-ion battery performance, ACS Omega 8 (2023) 5893–5900.
- [27] V. Sama, Synthesis and Characterization of CexTi1-xO2 Nanostructures, Chemistry, Youngstown State University, 2013, p. 115.
- [28] L.B. Arruda, C.M. Santos, M.O. Orlandi, W.H. Schreiner, P.N. Lisboa-Filho, Formation and evolution of TiO2 nanotubes in alkaline synthesis, Ceram. Int. 41 (2015) 2884–2891.
- [29] S. Azam, Z. Wei, R. Wang, Cerium oxide nanorods anchored on carbon nanofibers derived from cellulose paper as effective interlayer for lithium sulfur battery, J. Colloid Interface Sci. 615 (2022) 417–431.
- [30] Z. Wei, R. Wang, Chemically etched GeO2-x nanorods with abundant surface defects as effective cathode additive for trapping lithium polysulfides in Li-S batteries, J. Colloid Interface Sci. 615 (2022) 527–542.
- [31] S. Lee, J.H. Noh, H.S. Han, D.K. Yim, D.H. Kim, J.-K. Lee, J.Y. Kim, H.S. Jung, K. S. Hong, Nb-doped TiO2: a new compact layer material for TiO2 dye-sensitized solar cells, J. Phys. Chem. C 113 (2009) 6878–6882.
- [32] X. Lü, X. Mou, J. Wu, D. Zhang, L. Zhang, F. Huang, F. Xu, S. Huang, Improved-performance dye-sensitized solar cells using Nb-doped TiO2 electrodes: efficient electron injection and transfer, Adv. Funct. Mater. 20 (2010) 509–515.
- [33] L. Kong, C. Wang, H. Zheng, X. Zhang, Y. Liu, Defect-induced yellow color in Nb-doped TiO2 and its impact on visible-light photocatalysis, J. Phys. Chem. C 119 (2015) 16623–16632.
- [34] A. Manole, M. Dobromir, M. Girtan, R. Mallet, G. Rusu, D. Luca, Optical properties of Nb-doped TiO2 thin films prepared by sol–gel method, Ceram. Int. 39 (2013) 4771–4776.
- [35] Y. Wang, B.M. Smarsly, I. Djerdj, Niobium doped TiO2 with mesoporosity and its application for lithium insertion, Chem. Mater. 22 (2010) 6624–6631.
- [36] L. Zhu, Q. Lu, L. Lv, Y. Wang, Y. Hu, Z. Deng, Z. Lou, Y. Hou, F. Teng, Ligand-free rutile and anatase TiO 2 nanocrystals as electron extraction layers for high performance inverted polymer solar cells, RSC Adv. 7 (2017) 20084–20092.
- [37] H.-B. Kim, D.-J. Jang, Morphological variation of anatase TiO 2 crystals via formation of titanium glycerolate precursors under microwave irradiation, CrystEngComm 17 (2015) 3325–3332.
- [38] S.S. Mali, C.A. Betty, P.N. Bhosale, P. Patil, Synthesis, characterization of hydrothermally grown MWCNT-TiO2 photoelectrodes and their visible light absorption properties, ECS Journal of Solid State Science and Technology 1 (2012) M15
- [39] C.C. Chen, Y.P. Fu, S.H. Hu, Characterizations of TiO2/SiO2/Ni–Cu–Zn ferrite composite for magnetic photocatalysts, J. Am. Ceram. Soc. 98 (2015) 2803–2811.
- [40] P. Pujar, D. Gupta, S. Mandal, High-performance low voltage operation of indium zinc tin oxide thin film transistors using chemically derived sodium β-alumina dielectric, J. Mater. Sci. Mater. Electron. 30 (2019) 9097–9105.
- [41] T. Siddiqui, S.F. Shaikh, S.S. Sangale, S.D. Raut, R.S. Mane, M. Ubaidullah, B. M. Thamer, A.M. Al-Enizi, B.B. Totawar, M.S. Samdani, Mesoporous carbon of

- carbonized human urine waste: a valuable heterogeneous catalyst for chromene and xanthene derivative synthesis, Catalysts 10 (2020) 1369.
- [42] M. Kalapsazova, R. Stoyanova, E. Zhecheva, G. Tyuliev, D. Nihtianova, Sodium deficient nickel–manganese oxides as intercalation electrodes in lithium ion batteries, J. Mater. Chem. A 2 (2014) 19383–19395.
- [43] M. Zubair, G. Li, B. Wang, L. Wang, H. Yu, Electrochemical kinetics and cycle stability improvement with Nb doping for lithium-rich layered oxides, ACS Appl. Energy Mater. 2 (2018) 503–512.
- [44] Y. Zeng, X. Guo, Z. Wang, J. Geng, H. Zhang, W. Song, H. Yu, Z. Shao, B. Yi, Highly stable nanostructured membrane electrode assembly based on Pt/Nb 2 O 5 nanobelts with reduced platinum loading for proton exchange membrane fuel cells, Nanoscale 9 (2017) 6910–6919.
- [45] M. Saha, S. Ghosh, S. Paul, B. Dalal, S.K. De, Nb-Dopant-Induced tuning of optical and electrical property of anatase TiO2 nanocrystals, %J ChemistrySelect 3 (2018) 6654–6664
- [46] M. Barawi, L. De Trizio, R. Giannuzzi, G. Veramonti, L. Manna, M. Manca, Dual band electrochromic devices based on Nb-doped TiO2 nanocrystalline electrodes, ACS Nano 11 (2017) 3576–3584.
- [47] H. Su, Y.-T. Huang, Y.-H. Chang, P. Zhai, N.Y. Hau, P.C.H. Cheung, W.-T. Yeh, T.-C. Wei, S.-P. Feng, The synthesis of Nb-doped TiO2 nanoparticles for improved-performance dye sensitized solar cells, Electrochim. Acta 182 (2015) 230–237.
- [48] J. Yang, X. Zhang, C. Wang, P. Sun, L. Wang, B. Xia, Y. Liu, Solar photocatalytic activities of porous Nb-doped TiO2 microspheres prepared by ultrasonic spray pyrolysis, Solid State Sci. 14 (2012) 139–144.
- [49] Z. Wei, J. Li, Y. Wang, R. Wang, High-performance Li-S batteries enabled by polysulfide-infiltrated free-standing 3D carbon cloth with CeO2 nanorods decoration, Electrochim. Acta 388 (2021), 138645.
- [50] Z. Wei, J. Li, R. Wang, Surface engineered polar CeO2-based cathode host materials for immobilizing lithium polysulfides in High-performance Li-S batteries, Appl. Surf. Sci. 580 (2022), 152237.
- [51] A. Ali, S. Sarwar, D.R. Pollard, Z. Wei, R. Wang, X. Zhang, A.J. Adamczyk, Systematic mapping of electrocatalytic descriptors for hybrid and non-hybrid molybdenum dichalcogenides with graphene support for cathodic hydrogen generation, J. Phys. Chem. C 126 (2022) 17011–17024.
- [52] S. Sarwar, M.-C. Lin, C. Amezaga, Z. Wei, E. Iyayi, H. Polk, R. Wang, H. Wang, X. Zhang, Ultrasensitive electrochemical biosensors based on zinc sulfide/graphene hybrid for rapid detection of SARS-CoV-2, Adv. Compos. Hybrid Mater. 6 (2023) 40
- [53] S. Azam, Z. Wei, R. Wang, Adsorption-catalysis design with cerium oxide nanorods supported nickel-cobalt-oxide with multifunctional reaction interfaces for anchoring polysulfides and accelerating redox reactions in lithium sulfur battery, J. Colloid Interface Sci. 635 (2023) 466–480.
- [54] Y. Yang, X. Li, R. Luo, X. Zhang, J. Fu, Y. Zheng, K. Huo, T. Zhou, A topochemically constructed flexible heterogeneous vanadium-based electrocatalyst for boosted conversion kinetics of polysulfides in Li–S batteries, Mater. Chem. Front. 5 (2021) 3830–3840.
- [55] Y. Wen, Z. Shen, J. Hui, H. Zhang, Q. Zhu, Co/CoSe junctions enable efficient and durable electrocatalytic conversion of polysulfides for high-performance Li–S batteries, Adv. Energy Mater. (2023), 2204345.

- [56] J. He, G. Hartmann, M. Lee, G.S. Hwang, Y. Chen, A. Manthiram, Freestanding 1T MoS 2/graphene heterostructures as a highly efficient electrocatalyst for lithium polysulfides in Li–S batteries, Energy Environ. Sci. 12 (2019) 344–350.
- [57] Z. Ye, Y. Jiang, L. Li, F. Wu, R. Chen, Enhanced catalytic conversion of polysulfide using 1D CoTe and 2D MXene for heat-resistant and lean-electrolyte Li–S batteries, Chem. Eng. J. 430 (2022), 132734.
- [58] S. Wang, Y. Wang, Y. Song, X. Jia, J. Yang, Y. Li, J. Liao, H. Song, Immobilizing polysulfide via multiple active sites in W18O49 for Li-S batteries by oxygen vacancy engineering, Energy Storage Mater. 43 (2021) 422–429.
- [59] K. Xiao, Z. Chen, Z. Liu, L. Zhang, X. Cai, C. Song, Z. Fan, X. Chen, J. Liu, Z.X. Shen, N-doped carbon sheets arrays embedded with CoP nanoparticles as highperformance cathode for Li-S batteries via triple synergistic effects, J. Power Sources 455 (2020), 227959.
- [60] Z. Wei, S. Sarwar, S. Azam, M.R. Ahasan, M. Voyda, X. Zhang, R. Wang, Ultrafast microwave synthesis of MoTe2@ graphene composites accelerating polysulfide conversion and promoting Li2S nucleation for high-performance Li-S batteries, J. Colloid Interface Sci. 635 (2023) 391–405.
- [61] S. Fahad, Z. Wei, A. Kushima, In-situ TEM observation of fast and stable reaction of lithium polysulfide infiltrated carbon composite and its application as a lithium sulfur battery electrode for improved cycle lifetime, J. Power Sources 506 (2021), 230175.
- [62] X. Yang, J. Luo, X. Sun, Towards high-performance solid-state Li-S batteries: from fundamental understanding to engineering design, Chem. Soc. Rev. 49 (2020) 2140–2195.
- [63] W.G. Lim, S. Kim, C. Jo, J. Lee, A comprehensive review of materials with catalytic effects in Li–S batteries: enhanced redox kinetics, Angew. Chem. Int. Ed. 58 (2019) 18746–18757.
- [64] Y. Song, W. Cai, L. Kong, J. Cai, Q. Zhang, J. Sun, Rationalizing electrocatalysis of Li–S chemistry by mediator design: progress and prospects, Adv. Energy Mater. 10 (2020), 1901075.
- [65] W. Yao, W. Zheng, J. Xu, C. Tian, K. Han, W. Sun, S. Xiao, ZnS-SnS@ NC Heterostructure as robust lithiophilicity and sulfiphilicity mediator toward highrate and long-life lithium-sulfur batteries, ACS Nano 15 (2021) 7114–7130.
- [66] W. Yao, C. Tian, C. Yang, J. Xu, Y. Meng, I. Manke, N. Chen, Z. Wu, L. Zhan, Y. Wang, P-Doped NiTe2 with Te-vacancies in lithium-sulfur batteries prevents shuttling and promotes polysulfide conversion, Adv. Mater. 34 (2022), 2106370.
- [67] W. Yao, J. Xu, Y. Cao, Y. Meng, Z. Wu, L. Zhan, Y. Wang, Y. Zhang, I. Manke, N. Chen, Dynamic intercalation–conversion site supported ultrathin 2D mesoporous SnO2/SnSe2 hybrid as bifunctional polysulfide immobilizer and lithium regulator for lithium–sulfur chemistry, ACS Nano 16 (7) (2022) 10783–10797.
- [68] Z. Barlow, Z. Wei, R. Wang, Surface and defect engineered polar titanium dioxide nanotubes as an effective polysulfide host for high-performance Li-S batteries, Mater. Chem. Phys. (2023), 128316.
- [69] Z. Wei, Lithium Polysulfide Battery with Improved Capacity and Cycle Performance Using Carbon Black Coated Free-Standing Carbon Cloth, 2019.
- [70] S. Azam, Z. Wei, R. Wang, Nickel Cobalt Oxide Decorated Cerium Oxide Nanorods for Polysulfide Trapping and Catalytic Conversion in Advanced Lithium Sulfur Batteries, ECS Meeting Abstracts, IOP Publishing, 2022, p. 539.